



Cite this: *Catal. Sci. Technol.*, 2023, 13, 6480

The quantitative contribution of interfacial coexisting Mn and O vacancies to MnO_2 photocatalytic degradation of phenol†

Yahui Zhou,‡ Xingxin Lei,‡ Dali Yan, Jian Ye, Bo Deng * and Weilin Xu

Vacancy engineering is an important means to improve the catalytic performance of photocatalysts. Both V_{Mn} and V_{O} can promote photocatalytic and thermocatalytic reactions of MnO_2 catalysts. From the point of view of reducing energy consumption, photocatalysis has incomparable advantages over thermocatalysis. Meanwhile, in-depth investigation of the relative contribution of V_{Mn} and V_{O} on the photocatalytic reaction was not concluded yet. In this paper, $V_{\text{Mn}}-1$ and $V_{\text{Mn}}-2$ (with different levels of manganese vacancies (V_{Mn})) and $V_{\text{Mn},\text{O}}$ (with both V_{Mn} and oxygen vacancies (V_{O})) were synthesized to investigate the relative contributions of V_{Mn} and V_{O} in the photocatalytic process by MnO_2 . The catalysts were characterized by EDS, ICP, and XPS to explore their structures and the concentrations of V_{Mn} and V_{O} . The contributions to phenol degradation were calculated to be 487321.43 (mg L^{-1}) phenol per mol V_{Mn} and 125917.16 (mg L^{-1}) phenol per mol V_{O} for 2 h irradiation under 400 mW cm^{-2} visible light. Density-functional theory (DFT) calculations were performed to explain the different contributions of V_{Mn} and V_{O} . The higher contribution of V_{Mn} is attributed to its induced formation of a continuous band gap on the (001) crystal surface, which is favourable for visible light absorption and carrier transport. This study provides theoretical guidance and research direction for the design of efficient photocatalysts using vacancy engineering.

Received 21st July 2023,
Accepted 20th September 2023

DOI: 10.1039/d3cy01005h

rsc.li/catalysis

1. Introduction

As a new type of clean energy utilization technology, photocatalysts have great application prospects in wastewater treatment,¹ CO_2 reduction and so on.² Common photocatalysts include TiO_2 ,³ ZnO ,⁴ $\text{g-C}_3\text{N}_4$,⁵ MOFs,⁶ MnO_2 and so on. However, it must be recognized that the catalytic efficiency of the current photocatalysts is still unable to meet the requirements for practical applications.⁷ Vacancy engineering is the most commonly used means to improve the catalytic performance of photocatalysts. Cationic vacancies are the positions where cationic elements in crystals are missing, and the vacancies formed by lattice oxygen escaping are known as V_{O} , also called anionic vacancies.^{8,9} Improving the catalytic performance of photocatalysts by introducing anionic and cationic vacancies has become a hot research topic in recent years. Zhang *et al.*¹⁰ constructed anionic and cationic vacancies on Bi_2WO_6 and found that its carrier separation efficiency was higher, which

enabled the catalyst to achieve higher catalytic efficiency. Wang *et al.*¹¹ constructed Bi_2WO_6 hollow microspheres with oxygen vacancies and found that their high catalytic effect originated from the fast charge transfer hindering carrier complexation. Ding *et al.*¹² constructed Ti vacancy-rich *p*- TiO_2 and found that its high photocatalytic efficiency was due to the stronger carrier separation and transport.

As a common photocatalyst, $\delta\text{-MnO}_2$ has a strong absorption capacity for light in the UV to IR range due to its inherently small bandgap, meaning that it also has a weak Mn–O bond making it easier to generate oxygen vacancies.¹³ In recent years, many studies have been conducted to improve the photocatalytic performance of MnO_2 by introducing anionic and cationic vacancies. Jiang *et al.*¹⁴ found that the introduction of V_{Mn} can promote the absorption of visible light and act as a capture center to facilitate the separation of carriers, improving the photocatalytic performance of MnO_2 . Zhang *et al.*¹⁵ used femtosecond transient absorption spectroscopy to study the decay of photogenerated vacancies in MnO_2 with different V_{Mn} contents and found that the introduction of appropriate V_{Mn} could prolong the lifetimes of photogenerated carriers which also illustrated the effect of the presence of V_{Mn} on the separation of carriers. Xu *et al.*¹⁶ calculated *via* density functional theory (DFT) that V_{Mn} generated by excess alkali

State Key Laboratory of New Textile Materials and Advanced Processing Technologies, Wuhan Textile University, Wuhan 430200, P.R. China.

E-mail: dengjianguo88@outlook.com

† Electronic supplementary information (ESI) available. See DOI: <https://doi.org/10.1039/d3cy01005h>

‡ Yahui Zhou and Xingxin Lei contributed equally to this work.

ions produces additional occupied states, increasing the carrier concentration and photocatalytic activity of MnO_2 photocatalysts. The introduction of V_O could promote the visible light absorption ability and increase the number of active sites for the reaction, thus improving the photocatalytic efficiency of MnO_2 .¹⁷ In addition, V_O can promote the light-induced separation of electron-hole pairs acting as an electron trap and reduce the complexation of electron-hole pairs.¹⁸ Both V_Mn and V_O can shrink the band gap of MnO_2 catalysts and then improve their light absorption performance and promote the separation of electron-hole pairs. Thus, the photocatalytic performance of MnO_2 could be significantly improved.¹⁹

It was reported that both V_Mn and V_O promote photocatalytic and thermocatalytic reactions of MnO_2 . From the point of view of reducing energy consumption, photocatalysis has incomparable advantages over thermocatalysis. Meanwhile, in-depth investigation of the relative contribution of V_Mn and V_O on the photocatalytic reaction was not concluded yet.

Phenol, represented by the phenolic pollutants, is a common organic pollutant in wastewater and has attracted widespread attention due to its strong toxicity at low concentrations.^{20,21} In this study, phenol was selected as a model pollutant to investigate the degree of contribution of V_O and V_Mn of $\delta\text{-MnO}_2$ photocatalysts to the degradation of phenol. $\text{V}_\text{Mn-1}$ and $\text{V}_\text{Mn-2}$ with different concentrations of V_Mn were prepared by the redox reaction between ammonium oxalate and potassium permanganate and then H_2O_2 was used to further etch the surface of $\text{V}_\text{Mn-2}$ to introduce V_O to form $\text{V}_\text{Mn,O}$.

2. Experimental section

2.1. Materials

All chemicals are of analytical grade and the water is deionized water. Potassium permanganate ($\geq 99.5\%$, KMnO_4) was purchased from Tianjin Tianda Chemical Reagent Factor. Ammonium oxalate ($\geq 99.5\%$, $(\text{NH}_4)_2\text{C}_2\text{O}_4$) was purchased from Shanghai Maclean Biochemical Technology Co. Anhydrous ethanol (AR) was purchased from SCR. Hydrogen peroxide ($\geq 30\%$, H_2O_2) and phenol ($\geq 99.0\%$) were purchased from Sinopharm Group Chemical Reagent Co.

2.2. Catalyst synthesis

Typically, 1.0 g of potassium permanganate and ammonium oxalate (1.8 g, 0.8 g) were added sequentially to a beaker containing 130 ml of deionized water, and the beaker was placed in a water bath at 90 °C with stirring for 10 h. After the reaction, the mixture in the beaker was cooled, filtered, and repeatedly rinsed with alcohol and deionized water several times. Finally, the precipitate was dried in a blast oven at 80 °C for 24 h. The samples obtained were named $\text{V}_\text{Mn-1}$ and $\text{V}_\text{Mn-2}$, respectively. 5 mL of H_2O_2 (30%) was added to 20 ml of deionized water, and then 60 mg of $\text{V}_\text{Mn-2}$ was added to the above-mixed solution and stirred at room temperature for 1 h. After that, the obtained samples were

Table 1 Specific reagent dosage for different samples

| Sample | $(\text{NH}_4)_2\text{C}_2\text{O}_4$ | KMnO_4 | H_2O_2 (30%) |
|------------------------|---------------------------------------|-----------------|------------------------------|
| $\text{V}_\text{Mn-1}$ | 1.8 g | 1.0 g | — |
| $\text{V}_\text{Mn-2}$ | 0.8 g | 1.0 g | — |
| $\text{V}_\text{Mn,O}$ | 0.8 g | 1.0 g | 5 ml |

washed, filtered, and oven-dried overnight, and the samples obtained were named $\text{V}_\text{Mn,O}$. The specific reagent dosage for different samples is shown in Table 1.

During the formation of $\delta\text{-MnO}_2$, a mixed state with a random distribution of Mn^{4+}O_6 and Mn^{3+}O_6 (ref. 22) will form due to the excess interlayer K^+ under the charge balance effect. At high-temperature, severely deformed Mn^{3+}O_6 will be readily reconstructed under increased lattice strain, and thus the Mn–O bond was broken. Finally, Mn^{3+} was detached and formed V_Mn .¹⁶

Therefore, MnO_2 was prepared using a hydrothermal reaction of 1 g of KMnO_4 with 0.8 g and 1.8 g of ammonium oxalate, respectively, with ammonium oxalate acting as the reducing agent. Relative to the 1 g ammonium oxalate system, MnO_2 produced with the 0.8 g ammonium oxalate system (with a lower concentration of MnO_2) has a relatively higher content of K^+ and tended to produce more V_Mn .²³

2.3. Catalysis measurements

The degradation reaction was carried out with 50 mL (100 mg L^{-1}) of phenol solution and 50 mg of catalyst powder, and the suspension was first magnetically stirred in the dark for 0.5 h to reach the adsorption–desorption equilibrium. The suspensions were irradiated under a visible xenon lamp with an optical power density of about 300 mW cm^{-2} . The temperature of the catalytic reaction was fixed at 30 °C to exclude the effect of thermal catalysis. A sample of 4 mL was taken every 30 min, and centrifuged to remove the catalyst, and the concentration of the phenol solution was analyzed using a UV-vis spectrophotometer at 270 nm.²⁴ The concentration of phenol and intermediate products was detected by HPLC (1220 infinity II, German).

2.4. Characterization

X-ray diffraction (XRD) analyses were performed using a Rigaku Dmax 2500 (Japan). The sample was scanned at a rate of 2° min^{-1} over a range of 10–90°. Scanning electron microscopy (SEM) and energy-dispersive X-ray spectroscopy (EDX) images were obtained using a scanning electron microscope (TESCAN MIRA LMS, Czech Republic). Raman spectral data were obtained using a Thermo DXR microlaser Raman system (USA) under 524 nm laser excitation. Brunauer–Emmett–Teller (BET) analysis data were obtained from N_2 adsorption–desorption data using a Maize ASAP2460 at 77 K. Photochemical measurements were performed using a CHI 630B workstation. Electron spin resonance (ESR) spectroscopy was carried out using a Bruker EMXPLUS (Germany). The electronic structure of the catalyst surface

elements was examined by X-ray photoelectron spectroscopy (XPS, Thermo Scientific ESCALAB 250Xi, USA). Total organic carbon (TOC) data in solution were obtained using a total organic carbon lysimeter (TOC-L, Jin Dao). The toxicity of intermediates was analysed *via* ECOSAR software prediction.

3. Results and discussion

3.1. The synthesis of V_{Mn-1} , V_{Mn-2} and $V_{Mn,O}$

The schematic diagram of the sample synthesis is shown in Fig. 1. According to the literature,²⁵ MnO_2 with different V_{Mn} samples was prepared by a simple redox reaction between ammonium oxalate and potassium permanganate. After etching by H_2O_2 , an unstable structure was formed on the surface of MnO_2 , leading to the separation of lattice oxygen and the formation of V_O . The formation of V_O on MnO_2 surfaces etched by H_2O_2 has been explained in detail by Yan *et al.*²⁶

3.2. The morphological and structural characteristics of V_{Mn-1} , V_{Mn-2} , and $V_{Mn,O}$

The morphological and structural characteristics of V_{Mn-1} , V_{Mn-2} , and $V_{Mn,O}$ are shown in Fig. 2. All samples show the shape of a nanoflower. Nanoflowers are formed by stacking multiple nanosheets (Fig. 2a, d and g). The V_{Mn-2} nanoflowers have different diameters (Fig. 2d and e), whereas the V_{Mn-1} nanospheres are more uniform in diameter and can be observed as entire spheres (Fig. 2a and b). After further treatment with H_2O_2 , the $V_{Mn,O}$ sample boundary becomes unclear (Fig. 2g and h), which may be related to the structural distortion caused by lattice oxygen escape. The TEM images of the sample are shown in Fig. 2c, f and i. The lattice stripe spacings of 3.5 Å and 2.3 Å correspond to the (002) and (100) crystal planes of δ - MnO_2 , respectively.²³

The crystalline structure information of V_{Mn-1} , V_{Mn-2} , and $V_{Mn,O}$ was further explored by the XRD characterization technique, as shown in Fig. 3. The peak intensities of the samples matched with the standard card of δ - MnO_2 (JCPDS No. 80-1098), which proved that all samples have a birnessite structure of the hexagonal phase.²⁷ The weaker intensities of

the XRD diffraction peaks of the three samples indicate the presence of more lattice distortions and defects.²⁸

Further observation reveals that the diffraction peaks of the crystalline surfaces are broad and low compared to V_{Mn-1} , which indicates that V_{Mn-2} produces more V_{Mn} defects. Generally, the smaller the half peak width the better the crystallinity of the sample, and thus $V_{Mn,O}$ has the worst crystallinity (Table 2). The broadening of the diffraction peaks of $V_{Mn,O}$ compared to V_{Mn-2} further indicates the lattice distortion of the sample after H_2O_2 treatment, which is consistent with the indistinct results of the $V_{Mn,O}$ boundary change after H_2O_2 treatment (Fig. 2g and h).

Lattice parameters and volume crystallite size of the samples are shown in Table 2.

The pore size distribution and the specific surface area of the samples were obtained by isothermal adsorption and desorption curve characterization of N_2 . All isothermal samples exhibited H_3 -lagged type III isotherm characteristics.²⁹ The pore size distribution shows that all the samples have pore sizes in the range of 3 to 5 nm (Fig. S1†).

3.3. The XPS and EPR characters of V_{Mn-1} , V_{Mn-2} , and $V_{Mn,O}$

The electronic structure of surface elements and the presence of oxygen vacancies can be characterized by XPS as shown in Fig. 4. The average oxidation state (AOS) is commonly used to evaluate compounds with mixed valence states and is calculated as follows: $AOS = 8.956 - 1.126 \times \Delta E$, where ΔE is the splitting energy of Mn 3s.³⁰ The splitting energies of the three samples V_{Mn-1} , V_{Mn-2} , and $V_{Mn,O}$ were 5.03, 5.06, and 5.11 eV, respectively. A smaller value of AOS indicates a higher content of Mn^{3+} on the surface of the sample.³¹ Fitting to the Mn2p orbitals, the peak near 643.0 eV belongs to Mn^{4+} and the peak near 642.0 eV belongs to Mn^{3+} . The levels and proportions of Mn^{3+} and Mn^{4+} in the three samples derived from XPS are summarized in Table 3. The increase of Mn^{3+} content in $V_{Mn,O}$ compared with V_{Mn-2} is due to the formation of V_O on the surface of $V_{Mn,O}$. To balance the electrostatic equilibrium, a fraction of Mn^{4+} loses electrons to Mn^{3+} ($O^{2-} - 2e^- + 2Mn^{4+} + 2e^- \rightarrow 2Mn^{3+} + V_O +$

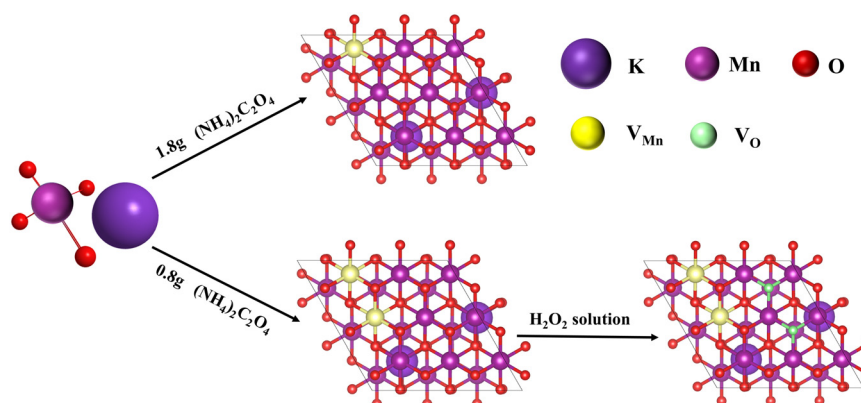


Fig. 1 The schematic diagram of the sample synthesis route.

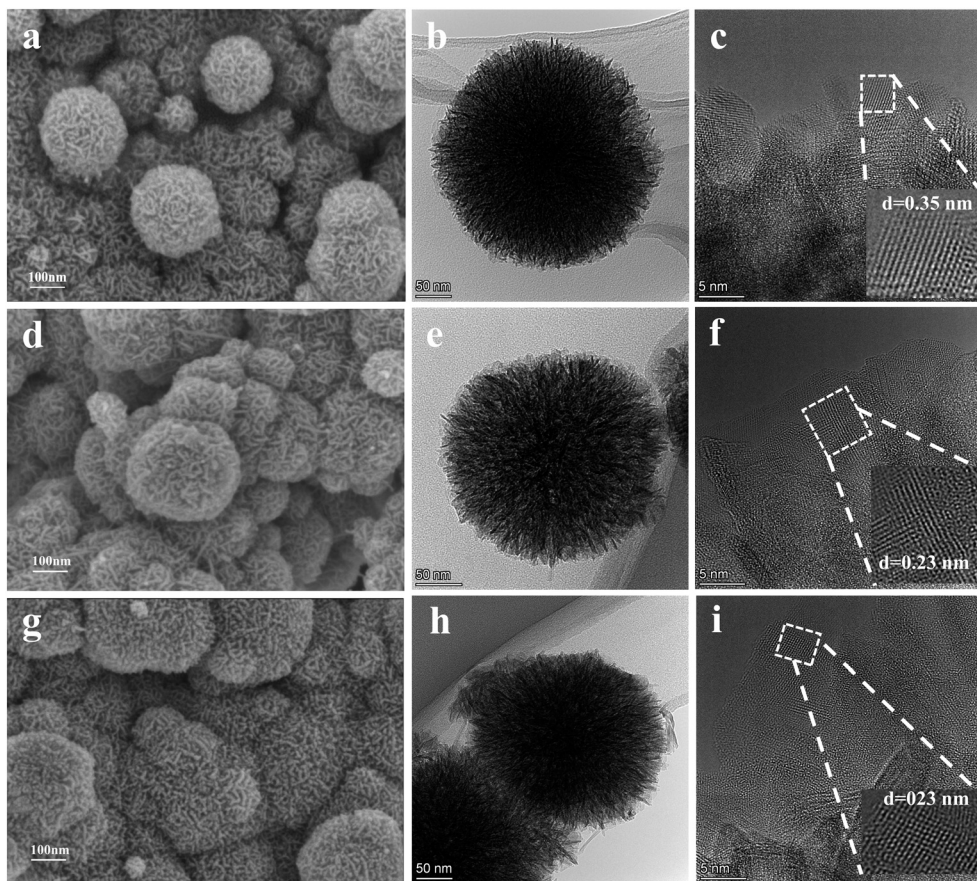


Fig. 2 SEM images of (a) V_{Mn-1} , (d) V_{Mn-2} , and (g) $V_{Mn,O}$, and TEM images of (b and c) V_{Mn-1} , (e and f) V_{Mn-2} , and (h and i) $V_{Mn,O}$.

$1/2O_2$). The representation of V_O is dedicated to the vacancy formed by the detachment of oxygen from the surface lattice.

Fitting the O 1s orbitals (Fig. 4b), the peaks at 529.88–529.74 eV correspond to lattice oxygen (O_{lat}), and the

peaks at 531.40–531.91 eV correspond to surface adsorbed oxygen (O_{abs}).³² V_O on the crystal surface can act as surface active sites to promote the adsorption and activation of gaseous oxygen, so the amount of O_{abs} will increase with the amount of V_O on the surface of the samples (Table 3).^{33,34} The increased content of O_{abs} in $V_{Mn,O}$ (37%) compared to V_{Mn-2} (28%) also indicates the successful introduction of V_O on the surface of $V_{Mn,O}$ after H_2O_2 etching. The elevated Mn^{4+} content on the surface of V_{Mn-2} compared to V_{Mn-1} is due to the increase in the K^+ content promoting the increase in the Mn^{4+} content, as reported in a former study.^{23,35}

The lattice oxygen peaks of V_{Mn-1} , V_{Mn-2} , and $V_{Mn,O}$ are located at 529.81, 529.88, and 529.74 eV, respectively. Some conclusions can also be drawn from the shifts in lattice oxygen peak positions. The O_{lat} peak of V_{Mn-2} is transferred to a position of high binding energy *versus* that of V_{Mn-1} due to the lower electron density around O_{lat} caused by the presence of V_{Mn} , which increases the binding energy of O_{lat} .²³ The O_{lat} peak of $V_{Mn,O}$ is moved toward a lower binding energy compared to that of V_{Mn-2} , implying that the interaction between Mn and O atoms is weaker. The presence of V_O results in an increase in the Mn^{3+} content, lengthening the Mn–O bond and thus reducing the binding energy of O_{lat} .^{36–38}

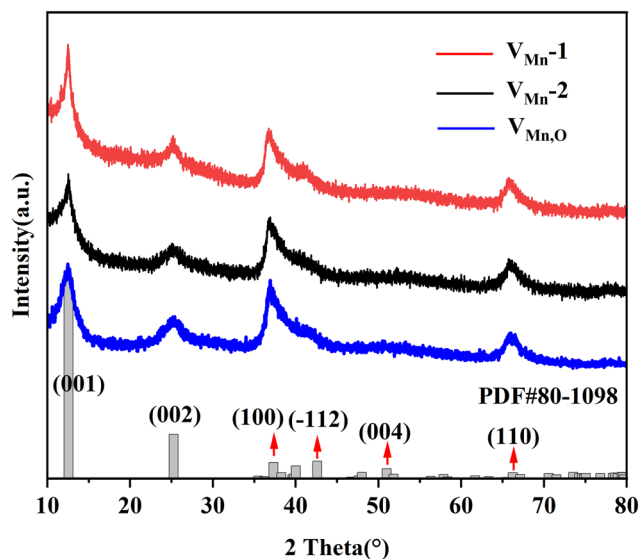
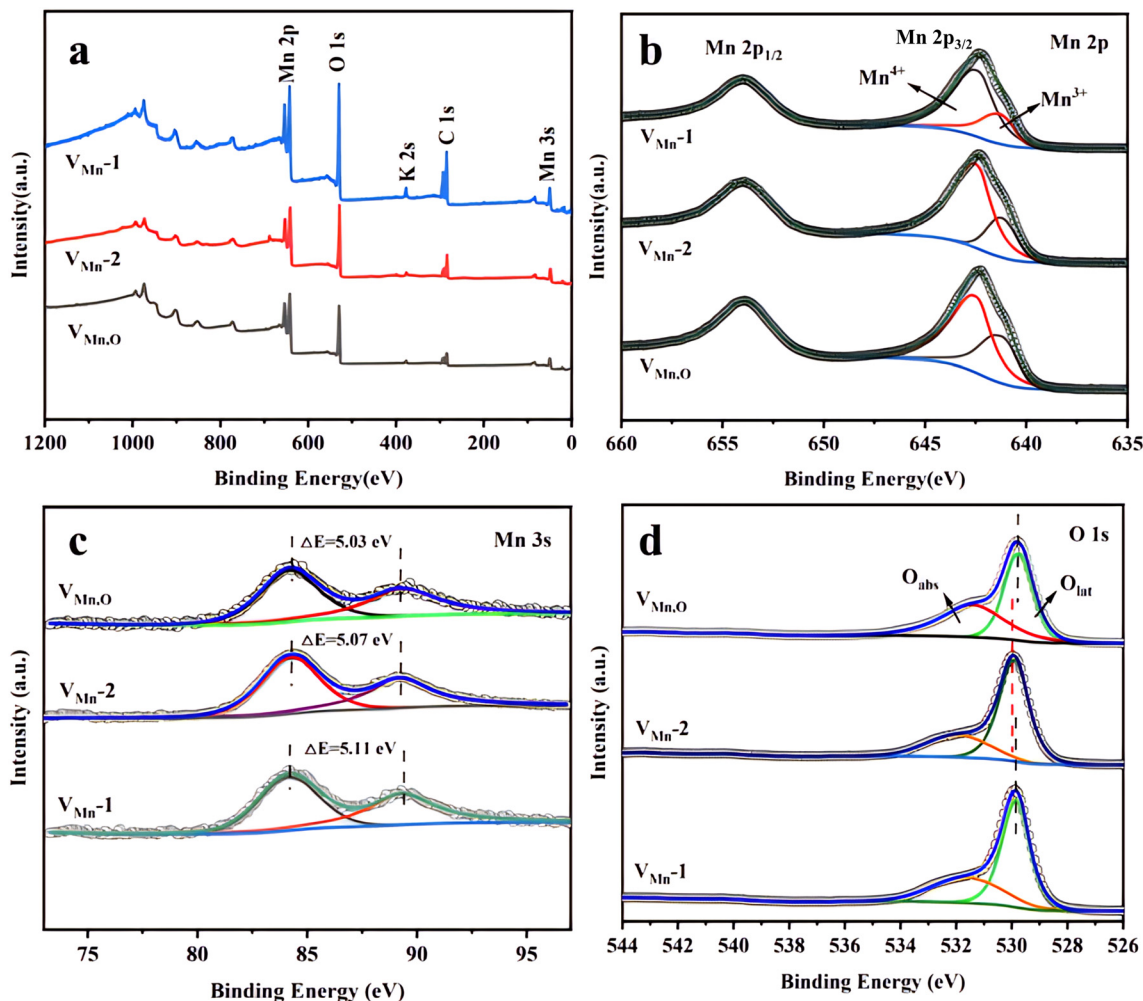


Fig. 3 XRD patterns of V_{Mn-1} , V_{Mn-2} , and $V_{Mn,O}$.

Table 2 The volume crystallite size, half-peak width (FWHM) and lattice parameters of the catalysts

| Sample | Volume crystallite size | FWHM | Lattice parameters (Å) |
|--------------------|-------------------------|-------|-----------------------------------|
| V _{Mn} O | 77 nm | 1.048 | $a = 5.149, b = 2.843, c = 7.176$ |
| V _{Mn} -2 | 58 nm | 0.929 | $a = 5.149, b = 2.843, c = 7.176$ |
| V _{Mn} -1 | 45 nm | 0.624 | $a = 5.149, b = 2.843, c = 7.176$ |

**Fig. 4** XPS spectra of V_{Mn}-1, V_{Mn}-2, and V_{Mn}O (a), Mn 2p (b), Mn 3s (c), and O 1s (d).

EPR is a frequently used means of characterizing the oxygen vacancy situation on the surface of a sample (Fig. 5), and signal intensity directly reflects the amount of V_O in the catalyst. The characteristic signal of V_O on the sample surface is reflected at $g = 2.003$, which is attributed to unpaired

electrons at the V_O site.^{39,40} The XPS and EPR results indicate that V_O was successfully introduced into the sample surface.

3.4. Chemical formula of V_{Mn}-1, V_{Mn}-2, and V_{Mn}O and distribution of V_O and V_{Mn}

Energy dispersive spectroscopy (EDS) (Fig. S2†) and XPS were used to characterize the Mn/O ratios in the different samples (Table 4). For all three samples, the Mn/O ratios were lower than the stoichiometry of MnO₂ (1:2), which confirms the presence of V_{Mn}, in concurrence with the results of Wang *et al.*²⁵ The results from ICP, EDS, and XPS revealed that the K/Mn ratios increased with the increase of V_{Mn}. This is because K⁺ is usually located in the interlayer to compensate

Table 3 Properties of different MnO₂ catalysts

| Catalysts | Mn | | | O | | AOS |
|--------------------|----------------------|----------------------|------------------------------------|----------------------|----------------------|------|
| | Mn ³⁺ (%) | Mn ⁴⁺ (%) | Mn ³⁺ /Mn ⁴⁺ | O _{abs} (%) | O _{lat} (%) | |
| V _{Mn} -1 | 0.31 | 0.69 | 0.45 | 0.31 | 0.69 | 5.11 |
| V _{Mn} -2 | 0.22 | 0.78 | 0.28 | 0.28 | 0.72 | 5.07 |
| V _{Mn} O | 0.39 | 0.61 | 0.52 | 0.37 | 0.63 | 5.03 |

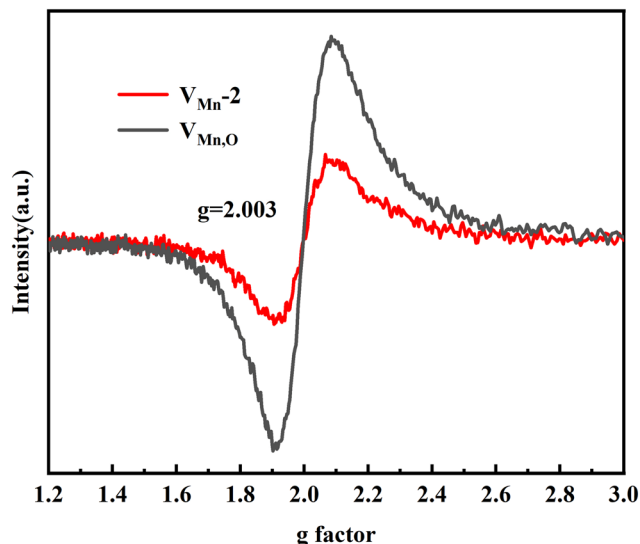


Fig. 5 EPR patterns of V_{Mn-2} and $V_{Mn,O}$.

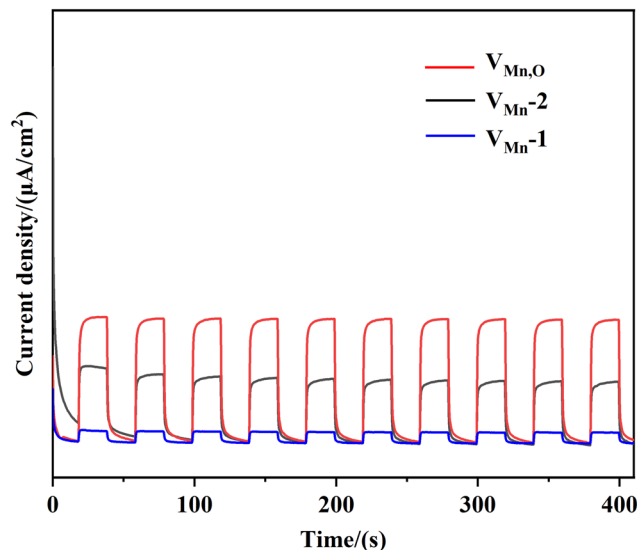


Fig. 6 The photocurrent responses of V_{Mn-1} , V_{Mn-2} , and $V_{Mn,O}$.

for the charge imbalance caused by V_{Mn} . Therefore, the K^+ content increases with the increase of the V_{Mn} content. The similar specific surface area of the samples makes it possible to ignore the effect on the catalytic efficiency due to the difference in specific surface area (Table 4). The photocatalytic reaction takes place mainly on the catalyst surface. The depth to which XPS can detect is approximately 8 nm to 10 nm. The Mn^{3+}/Mn^{4+} of $V_{Mn,O}$ is higher in comparison to that of V_{Mn-2} , indicating the successful formation of V_O on the surface of $V_{Mn,O}$ after treatment with H_2O_2 . The higher K/Mn obtained from XPS than that from ICP shows that K^+ is mainly concentrated in the surface layer of the catalyst. It also shows that V_{Mn} is mainly formed on the surface of the catalyst.

3.5. Catalytic performance of V_{Mn-1} , V_{Mn-2} , and $V_{Mn,O}$ and contribution of V_O and V_{Mn}

Carrier separation efficiency characterised by photocurrent response curves. Fig. 6 shows the photocurrent response curves of the V_{Mn-1} , V_{Mn-2} , and $V_{Mn,O}$.⁴⁰ The strength of photocurrent intensity is $V_{Mn,O} > V_{Mn-2} > V_{Mn-1}$, indicating the lowest complexation rate of electro-optically excited charge carriers in $V_{Mn,O}$. A similar phenomenon of enhanced

carrier separation due to the interfacial coexistence of Ti and O vacancies has been reported by Lu *et al.*⁴¹ Wang *et al.* reported a MnO_2 nanosheet with $V_{Mn,O}$, which showed semi-metallic properties.²⁵ The semi-metallic material has high photogenerated carrier response and high conductivity, which facilitates carrier mobility and separation.⁴² The photocurrent results are consistent with the photocatalytic experimental results (Fig. 6), and the $V_{Mn,O}$ activity is higher than that of V_{Mn-2} and V_{Mn-1} .⁴³

To assess the catalytic activity of the samples (Fig. 7), a phenol solution was chosen as a model contaminant. Phenol degradation followed the proposed primary reaction kinetics $\ln(C/C_0) = -kt$ (Fig. 7a), where C_0 and C are the concentrations of phenol ($mg\ L^{-1}$) at reaction times 0 and t (min), respectively, and k is the proposed primary rate constant (min^{-1}). The k values were calculated to be $0.00074\ min^{-1}$, $0.00105\ min^{-1}$, and $0.00150\ min^{-1}$ for the V_{Mn-1} , V_{Mn-2} , and $V_{Mn,O}$ samples, respectively. Fig. 7b shows the removal of total organic carbon (TOC) in the reaction, which demonstrates the production of by-products in the reaction. The reactive oxygen species (ROS) of $V_{Mn,O}$ were determined by EPR⁴⁴ (Fig. 7c), and the 3, 4 and 7 characteristic peaks correspond to the singlet oxygen (1O_2), hydroxyl radical

Table 4 Specific surface area, pore volume, XPS data, and chemical formula of the samples

| Catalysts | BET ($m^2\ g^{-1}$) | Pore volume ($cm^3\ g^{-1}$) | K/Mn | | | Mn/O | | Chemical formula ^a |
|------------|-----------------------|--------------------------------|------|------|------|----------|----------|--|
| | | | ICP | EDX | XPS | EDX | XPS | |
| V_{Mn-1} | 146.46 | 0.171 | 0.09 | 0.13 | 0.14 | 0.99 : 2 | 0.98 : 2 | $K_{0.09}Mn_{0.98}V_{Mn0.02}O_2$ |
| V_{Mn-2} | 127.95 | 0.165 | 0.12 | 0.17 | 0.19 | 0.48 : 2 | 0.96 : 2 | $K_{0.11}Mn_{0.96}V_{Mn0.04}O_2$ |
| $V_{Mn,O}$ | 139.83 | 0.209 | 0.12 | 0.16 | 0.20 | 1.11 : 2 | 0.95 : 2 | $K_{0.11}Mn_{0.96}V_{Mn0.04}O_{1.97}V_{O0.03}$ |

^a The chemical formula were gained according to elemental analysis (ICP) and XPS; V_{Mn} means the Mn vacancy, and V_O means the O vacancy.

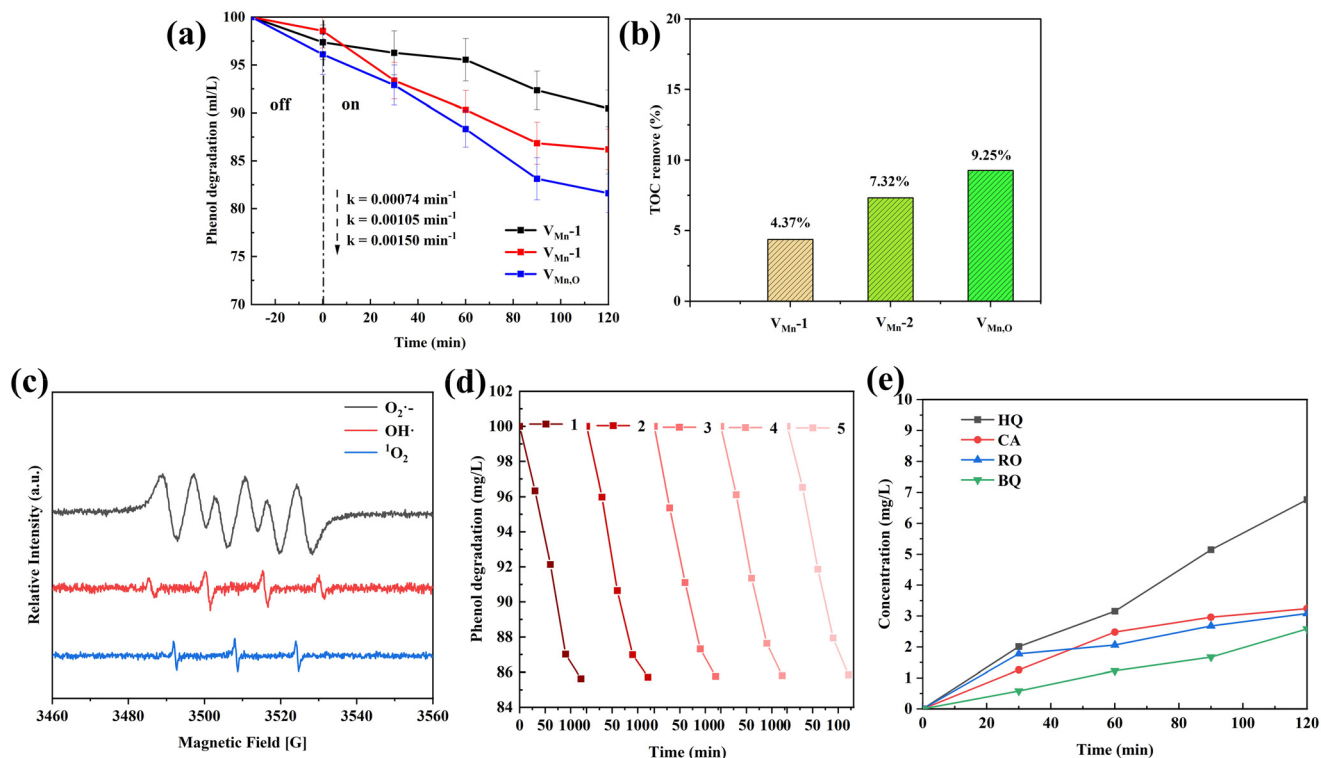


Fig. 7 (a) Concentration of phenol versus photocatalytic reaction time; (b) TOC removal; (c) ESR spectra of $O_2^{\cdot-}$, OH^{\cdot} , and 1O_2 ; (d) photocatalytic performance of $V_{Mn,O}$ after 5 degradation cycles; (e) possible intermediates of phenol degradation.

(OH^{\cdot}), and superoxide anion ($O_2^{\cdot-}$), respectively. After experiments on five catalytic cyclic reactions of $V_{Mn,O}$, and rinsing of $V_{Mn,O}$ with deionized water at the end of each catalytic reaction followed by drying at 100°C , it was found that $V_{Mn,O}$ maintained stable catalytic activity after five cycles of catalytic reactions (Fig. 7d). A comparison table with similar studies was added into the revised ESI† as shown in Table S1. HPLC was used to identify the possible intermediates of phenol degradation. Catechol

(CA), hydroquinone (HQ), benzoquinone (BQ), and resorcinol (RO) were identified *via* retention time (Fig. 7e).

The toxicity of the intermediates of phenol degradation was assessed using ECOSAR software as shown in Fig. 8. Detailed data are presented in Table S2.† Some intermediates are still toxic but can be completely degraded by prolonging the degradation time.

The molar masses of the samples (M) and the amounts of substances (n) of V_{Mn} and V_O in 50 mg of samples were

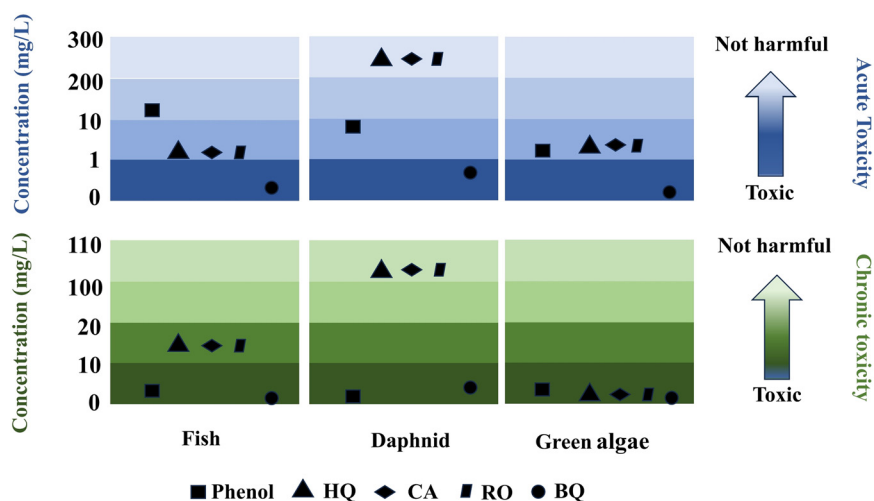


Fig. 8 The toxicity assessment of phenol intermediates.

Table 5 Catalytic performance of different MnO₂ catalysts

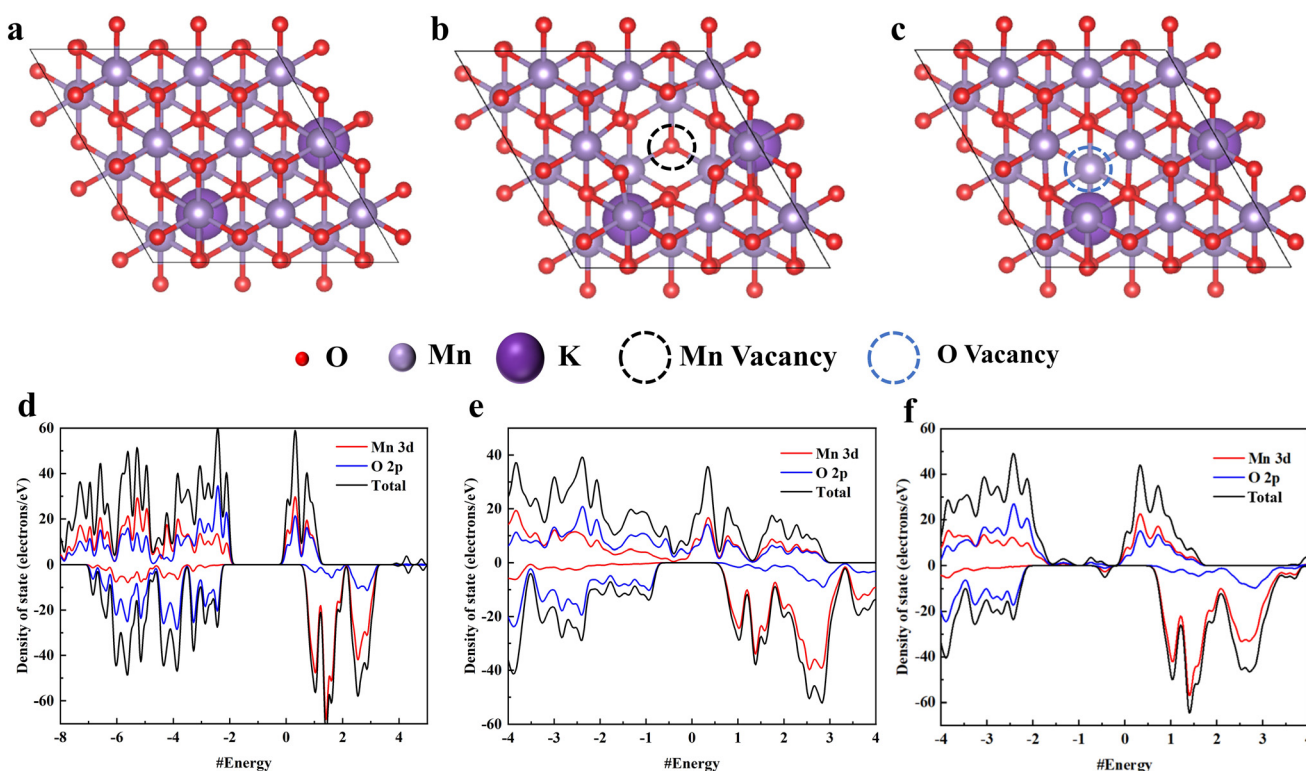
| Catalysts | Chemical formula | <i>M</i> (g mol ⁻¹) | Phenol degradation | <i>n</i> (mol) | Contribution | |
|--------------------|---|---------------------------------|------------------------------|---------------------------------------|----------------------------------|---|
| | | | | | Degradation | <i>k</i> |
| V _{Mn} -1 | K _{0.09} Mn _{0.98} V _{Mn0.02} O ₂ | 89.41 | 6.90 (mg L ⁻¹) | 1.12×10^{-5} V _{Mn} | 487 321.43 (mg L ⁻¹) | 27.68 min ⁻¹ mol ⁻¹ V _{Mn} |
| V _{Mn} -2 | K _{0.11} Mn _{0.96} V _{Mn0.04} O ₂ | 89.09 | 12.358 (mg L ⁻¹) | 2.24×10^{-5} V _{Mn} | phenol per mol V _{Mn} | |
| V _{Mn,O} | K _{0.11} Mn _{0.96} V _{Mn0.04} O _{1.97} V _{O0.03} | 88.61 | 14.486 (mg L ⁻¹) | 1.69×10^{-5} V _O | 125 917.16 (mg L ⁻¹) | 26.63 min ⁻¹ mol ⁻¹ V _O |
| | | | | | phenol per mol V _O | |

determined from the chemical formula of the three samples (Table 4), and the contribution ratios of the average V_{Mn} and V_O per mole to the catalytic performance and the reaction rate constant (*k*) were further calculated, as shown in Table 5. A detailed calculation procedure is given in the ESI† (calculation process). The contribution of V_{Mn} per mole to phenol degradation was 487 321.43 mg L⁻¹ and the contribution of V_O per mole to phenol degradation was 125 917.16 mg L⁻¹ under visible light irradiation at 400 mW cm⁻² for 2 h.

To further analyze the reasons for the different contributions in the degradation efficiency of phenol by V_{Mn} and V_O respectively, we performed first-principles calculations based on DFT. The details of the calculation are provided in the ESI† (models and computational methods). The XRD results suggest that (001) is the main exposed surface of the sample, and the Wulff structure of δ-MnO₂ further proves that (001) is the main exposed surface of the crystal (Fig. S3†). Therefore, we constructed the perfect (001) MnO₂, Mn vacancy (001) MnO₂, and O vacancy (001) MnO₂ models respectively to study the energy band structure and

properties of the samples (Fig. S4†). Fig. 9 shows the (a) perfect (001) MnO₂, (b) Mn vacancy (001) MnO₂, and (c) O vacancy (001) MnO₂, and the (d–f) corresponding densities of states (DOS). The corresponding energy band diagrams of the samples are shown in the ESI (Fig. S5†). Compared with the perfect (001) MnO₂, both the Mn vacancy (001) MnO₂ and O vacancy (001) MnO₂ have reduced band gaps, and both show occupied states in the forbidden band. The local density of states (PDOS) of K⁺ was further investigated and it was found that K⁺ is hardly involved in contributing to the impurity energy level (Fig. S6†). The occupied states in the forbidden band are favorable for fast carrier transport and increased carrier concentration, but the Mn vacancy (001) MnO₂ exhibits a half-metal abundance with a zero-band gap and better carrier transport capability.⁴⁵ Because of the presence of a continuous band gap, the latter has a better phenol degradation rate than the former. This result also agrees with the results of phenol degradation efficiency during the actual experiment.

MnO₂ formed a continuous band gap after the introduction of V_{Mn}, thus improving its catalytic efficiency, a phenomenon reported in the literature,⁴⁵ where the

**Fig. 9** Top views of V_{Mn}-1, V_{Mn}-2, and V_{Mn,O} (a–c) and their corresponding densities of states (DOS) (d–f).

continuous band gap formed by V_{Mn} allows MnO_2 to utilize more sunlight and promotes photogenerated carrier production, thus improving its photocatalytic ability. Therefore, V_{Mn} has higher catalytic activity compared to V_O .⁴⁶

According to the existing literature, the main principle of photocatalytic reaction is that light excites the electrons in the valence band to the conduction band, leaving holes in the valence band, and the electron-hole pairs migrate to the surface of the photocatalyst for redox reactions with pollutants. The valence band (VB), which is fully occupied by electrons, is mainly composed of O 2p orbitals, whereas the conduction band (CB) is composed of Mn 3d orbitals in MnO_2 .⁴⁷ The introduction of V_{Mn} and V_O on MnO_2 will only change the orbital compositions of Mn 3d and O 2p in MnO_2 , respectively, and therefore we conclude that V_{Mn} and V_O do not interact. The same conclusion was demonstrated on ref. 10, where the introduction of anionic vacancies only improves the carrier separation, and no interaction is reported.

Conclusions

MnO_2 samples with different V_{Mn} concentrations (V_{Mn-1} and V_{Mn-2}) were prepared by adjusting the reaction conditions of ammonium oxalate and potassium permanganate, and V_O was introduced on the surface of V_{Mn-2} by the oxidation of H_2O_2 . The contribution of a single mole of V_{Mn} and V_O to phenol degradation was calculated by combining the results of actual photocatalytic degradation kinetics of phenol, and the contribution of each mole of V_{Mn} and V_O to phenol degradation was 487 321.43 mg L⁻¹ and 125 917.16 mg L⁻¹ under visible light irradiation at 300 mW cm⁻² for 2 h. The results of the simulations showed that the Mn vacancy (001) MnO_2 exhibits high photogenerated carrier responsiveness with zero band gap semi-metallic properties and facilitates carrier migration and separation. Quantifying the contributions of V_{Mn} and V_O in the photocatalytic degradation process of MnO_2 is important for exploring more efficient and sustainable MnO_2 photocatalysts.

Author contributions

Yahui Zhou and Xingxin Lei contributed equally to this work. The experiments were conducted by Yahui Zhou and Xingxin Lei. Other authors participated in the data analyses.

Conflicts of interest

The authors declare that they have no known competing financial interests or personal relationships that could have appeared to influence the work reported in this paper.

Acknowledgements

This work was supported by the National Science Foundation of China (No. U21A2095), the Key Research and Development Program of Hubei Province (No. 2021BAA068), The

Department of Education of Guangdong Province (2019GZDXM006) and the Foundation of State Key Laboratory of Coal Combustion (FSKLCCA2109).

References

- 1 M. R. Al-Mamun, S. Kader, M. S. Islam and M. Z. H. Khan, *J. Environ. Chem. Eng.*, 2019, **7**, 103248.
- 2 J. Ran, M. Jaroniec and S. Qiao, *Adv. Mater.*, 2018, **30**, 1704649.
- 3 N. Shehzad, M. Tahir, K. Johari, T. Murugesan and M. Hussain, *J. CO₂ Util.*, 2018, **26**, 98–122.
- 4 A. Sharma, A. Hosseini-Bandegharai, N. Kumar, S. Kumar and K. Kumari, *J. CO₂ Util.*, 2022, **65**, 102205.
- 5 T. Xiong, W. Cen, Y. Zhang and F. Dong, *ACS Catal.*, 2016, **6**, 2462–2472.
- 6 Q. Wang, Q. Gao, A. M. Al-Enizi, A. Nafady and S. Ma, *Inorg. Chem. Front.*, 2020, **7**, 300–339.
- 7 R. Ji, M. Zhang, W. Ma, Z. Zhu, C. Ma, P. Huo, Y. Yan, Y. Liu and C. Li, *J. Taiwan Inst. Chem. Eng.*, 2019, **97**, 158–169.
- 8 W. Long, M. U. Hamza, M. N. Abdul-Fattah, A. M. Rheima, Y. M. Ahmed, F. S. Fahim, U. S. Altimari, A. K. O. Aldulaim, B. J. Janani and A. Fakhri, *Colloids Surf., A*, 2022, **650**, 129468.
- 9 M. Wang, M. Shen, X. Jin, J. Tian, M. Li, Y. Zhou, L. Zhang, Y. Li and J. Shi, *ACS Catal.*, 2019, **9**, 4573–4581.
- 10 X. Zhang, Y. Zhang, H. Li, Y. Wang, M. Xiang, W. Yu, H. Huang and H. Ou, *Appl. Surf. Sci.*, 2022, **602**, 154311.
- 11 T. Wang, C. Feng, J. Liu, D. Wang, H. Hu, J. Hu, Z. Chen and G. Xue, *Chem. Eng. J.*, 2021, **414**, 128827.
- 12 W. Ding, X. Li, S. Su, Z. Liu, Y. Cao, L. Meng, S. Yuan, W. Wei and M. Luo, *Nanoscale*, 2023, **15**, 4014–4021.
- 13 S. Das, A. Samanta and S. Jana, *ACS Sustainable Chem. Eng.*, 2017, **5**, 9086–9094.
- 14 G. Li, C. Mang, J. Luo, M. Rao, Z. Peng and T. Jiang, *J. Colloid Interface Sci.*, 2022, **618**, 229–240.
- 15 H. Zhang, S. Rong and P. Zhang, *ACS Appl. Mater. Interfaces*, 2021, **13**, 18944–18953.
- 16 L. Niu, L. Yan, Z. Lu, Y. Gong, T. Chen, C. Li, X. Liu and S. Xu, *J. Energy Chem.*, 2021, **56**, 245–258.
- 17 J. Zhao, Y. Wang, N. Li, S. Wang, J. Yu and X. Li, *Chemosphere*, 2021, **276**, 130257.
- 18 D. Ding, Y. Zhou, T. He and S. Rong, *Chem. Eng. J.*, 2022, **431**, 133737.
- 19 S. Panimalar, S. Logambal, R. Thambidurai, C. Inmozhi, R. Uthrakumar, A. Muthukumaran, R. A. Rasheed, M. K. Gatasheh, A. Raja, J. Kennedy and K. Kaviyarasu, *Environ. Res.*, 2022, **205**, 112560.
- 20 A. Mehta, A. Mishra and S. Basu, *Environ. Sci.: Water Res. Technol.*, 2018, **4**, 2012–2020.
- 21 Y. Shi, M. Zhang, Y. Li, G. Liu, R. Jin, Q. Wang, H. Xu and S. Gao, *Ceram. Int.*, 2020, **46**, 25905–25914.
- 22 Y. Yuan, K. He, B. W. Byles, C. Liu, K. Amine, J. Lu, E. Pomerantseva and R. Shahbazian-Yassar, *Chem.*, 2019, **5**, 1793–1805.

- 23 J. Wang, J. Li, C. Jiang, P. Zhou, P. Zhang and J. Yu, *Appl. Catal., B*, 2017, **204**, 147–155.
- 24 Y. Wang, H. Sun, H. M. Ang, M. O. Tadé and S. Wang, *Appl. Catal., B*, 2015, **164**, 159–167.
- 25 H. Wang, J. Zhang, X. Hang, X. Zhang, J. Xie, B. Pan and Y. Xie, *Angew. Chem.*, 2015, **127**, 1211–1215.
- 26 L. Yan, C. Shen, L. Niu, M. Liu, J. Lin, T. Chen, Y. Gong, C. Li, X. Liu and S. Xu, *ChemSusChem*, 2019, **12**, 3571–3581.
- 27 J. Ji, X. Lu, C. Chen, M. He and H. Huang, *Appl. Catal., B*, 2020, **260**, 118210.
- 28 F. Liu, S. Rong, P. Zhang and L. Gao, *Appl. Catal., B*, 2018, **235**, 158–167.
- 29 G. Wang, Z. Ma, G. Zhang, C. Li and G. Shao, *Electrochim. Acta*, 2015, **182**, 1070–1077.
- 30 S. Wu, H. Liu, Z. Huang, H. Xu and W. Shen, *Appl. Catal., B*, 2022, **312**, 121387.
- 31 J. Gao, C. Jia, L. Zhang, H. Wang, Y. Yang, S.-F. Hung, Y.-Y. Hsu and B. Liu, *J. Catal.*, 2016, **341**, 82–90.
- 32 L. Zhu, J. Wang, S. Rong, H. Wang and P. Zhang, *Appl. Catal., B*, 2017, **211**, 212–221.
- 33 R. Yang, S. Peng, B. Lan, M. Sun, Z. Zhou, C. Sun, Z. Gao, G. Xing and L. Yu, *Small*, 2021, **17**, 2102408.
- 34 P. Cui, Y. Zhang, Z. Cao, Y. Liu, Z. Sun, S. Cheng, Y. Wu, J. Fu and E. Xie, *Chem. Eng. J.*, 2021, **412**, 128676.
- 35 S. Rong, K. Li, P. Zhang, F. Liu and J. Zhang, *Catal. Sci. Technol.*, 2018, **8**, 1799–1812.
- 36 H. Huang and D. Y. C. Leung, *ACS Catal.*, 2011, **1**, 348–354.
- 37 Y. Li, C. Zhang, H. He, J. Zhang and M. Chen, *Catal. Sci. Technol.*, 2016, **6**, 2289–2295.
- 38 Z. Yang, H. Du, S. Qu, Y. Hou, H. Ma, J. Wang, J. Wang, X. Wei and Z. Xu, *J. Mater. Chem. A*, 2016, **4**, 13778–13785.
- 39 Z. Barbieriková, D. Dvoranová, M.-V. Sofianou, C. Trapalis and V. Brezová, *J. Catal.*, 2015, **331**, 39–48.
- 40 H. Hirakawa, M. Hashimoto, Y. Shiraishi and T. Hirai, *ACS Catal.*, 2017, **7**, 3713–3720.
- 41 Y. Lu, Y.-X. Liu, L. He, L.-Y. Wang, X.-L. Liu, J.-W. Liu, Y.-Z. Li, G. Tian, H. Zhao, X.-H. Yang, J. Liu, C. Janiak, S. Lenaerts, X.-Y. Yang and B.-L. Su, *Nanoscale*, 2020, **12**, 8364–8370.
- 42 F. Ichihara, F. Sieland, H. Pang, D. Philo, A.-T. Duong, K. Chang, T. Kako, D. W. Bahnemann and J. Ye, *J. Phys. Chem. C*, 2020, **124**, 1292–1302.
- 43 D. Lagarde, L. Bouet, X. Marie, C. R. Zhu, B. L. Liu, T. Amand, P. H. Tan and B. Urbaszek, *Phys. Rev. Lett.*, 2014, **112**, 047401.
- 44 W. Ding, X. Li, S. Su, Z. Liu, Y. Cao, L. Meng, S. Yuan, W. Wei and M. Luo, *Nanoscale*, 2023, **15**, 4014–4021.
- 45 W. Yang, Y. Zhu, F. You, L. Yan, Y. Ma, C. Lu, P. Gao, Q. Hao and W. Li, *Appl. Catal., B*, 2018, **233**, 184–193.
- 46 S. Anandan, N. Ohashi and M. Miyauchi, *Appl. Catal., B*, 2010, **100**, 502–509.
- 47 Y. Li, F. Liu, X. Xu, Y. Liu, Y. Li, H. Ding, N. Chen, H. Yin, H. Lin, C. Wang and A. Lu, *Geochim. Cosmochim. Acta*, 2019, **256**, 116–134.